Collinear order in the spin-$\frac{5}{2}$ triangular-lattice antiferromagnet Na$_3$Fe(PO$_4$)$_2$

Sebin J. Sebastian [1] S. S. Islam,[1] A. Jain,[2] S. M. Yusuf [2] M. Uhlarz,[3] and R. Nath [1,*]

[1]*School of Physics, Indian Institute of Science Education and Research Thiruvananthapuram, Kerala 695551, India*
[2]*Solid State Physics Division, Bhabha Atomic Research Centre, Mumbai 400 085, India*
[3]*Dresden High Magnetic Field Laboratory (HLD-EMFL), Helmholtz-Zentrum Dresden-Rossendorf, 01328 Dresden, Germany*

We set forth the structural and magnetic properties of the frustrated spin-5/2 triangle lattice antiferromagnet Na$_3$Fe(PO$_4$)$_2$ examined via x-ray diffraction, magnetization, heat capacity, and neutron diffraction measurements on the polycrystalline sample. No structural distortion was detected from the temperature-dependent x-ray diffraction down to 12.5 K, except a systematic lattice contraction. The magnetic susceptibility at high temperatures agrees well with the high-temperature series expansion for a spin-5/2 isotropic triangular lattice antiferromagnet with an average exchange coupling of $J/k_B \simeq 1.8$ K rather than a one-dimensional spin-5/2 chain model. This value of the exchange coupling is consistently reproduced by the saturation field of the pulse field magnetization data. It undergoes a magnetic long-range order at $T_N \simeq 10.4$ K. Neutron diffraction experiments elucidate a collinear antiferromagnetic ordering below T_N with the propagation vector $k = (1, 0, 0)$. An intermediate value of frustration ratio ($f \simeq 3.6$) reflects moderate frustration in the compound which is corroborated by a reduced ordered magnetic moment of $\sim$1.52μ_B at 1.6 K, compared to its classical value (5μ_B). Magnetic isotherms exhibit a change of slope envisaging a field induced spin-flop transition at $H_{SF} \simeq 3.2$ T. The magnetic field vs temperature phase diagram clearly unfold three distinct phase regimes, reminiscent of a frustrated magnet with in-plane (XY-type) anisotropy.

I. INTRODUCTION

Triangular-lattice antiferromagnet (TLA) is a simple example of geometrically frustrated magnets which has been a motif since the advent of various exotic quantum phases including quantum spin-liquid (QSL) [1,2]. Ideally, two-dimensional (2D) TLAs with isotropic (Heisenberg) exchange interaction undergo a noncollinear 120° ordering irrespective of their spin value [3–7]. However, in real materials the inherent exchange anisotropy and interlayer couplings often have broad implications, leading to more complex and nontrivial ground states [8]. For instance, for TLAs with easy-axis anisotropy, the low temperature 120° state is often preceded by a collinear state in zero field, as in Ba$_3$(Mn, Co)Nb$_2$O$_9$ and other TLA compounds [9–17], while for systems with easy-plane anisotropy, the collinear phase is unstable and entails only 120° ordering [18,19]. The materials with noncollinear magnetic structure give rise to spin chirality, a wellspring of strong magnetoelectric coupling [20]. Moreover, a spatially anisotropic spin-1/2 TLA model has been proposed to host QSL phase for a critical value of the ratio of exchange couplings [21–23]. Recently, an extended fluctuating regime with slow dynamics below magnetic ordering is detected in the spin-3/2 isotropic TLAs [24]. Overall, diverse phase regimes are anticipated in TLAs while going from a classical (high spin) to quantum (low spin) limit owing to the geometrical frustration in concurrence with magnetic anisotropy, effect of quantum fluctuations, etc. [25,26].

Recently, a series of compounds with general formula $AA'M(XO_4)_2$ (A = Ba, K, Rb, and Sr, A' = Na$_2$ and Ag$_2$, M = Mn, Ni, Co, Cr, and Cu, and X = P and V) are reported with varying crystal structures [27–35]. Interestingly, this series of compounds are projected as low-dimensional spin systems where the superexchange takes place in an elongated path involving VO$_4$ or PO$_4$ units. Though the majority of the compounds in this series are described in terms of an anisotropic triangular lattice model, some of them are found to be exceptions. BaAg$_2$Cu(VO$_4$)$_2$ with triclinic ($P\bar{1}$) structure was initially proposed to be a spin-1/2 anisotropic triangular lattice system, due to its unequal Cu–Cu bond lengths [28]. Subsequently, the band structure calculations ruled out this proposal and established a superposition of double spin-1/2 chains: one is ferromagnetic and another is antiferromagnetic [35]. Similarly, the monoclinic ($C2/c$) compound BaNa$_2$Cu(VO$_4$)$_2$ features antiferromagnetic spin-1/2 crossed chains arranged 62° with respect to each other [27]. Moreover, the signature of QSL is reported in the structurally perfect spin-1/2 TLA BaNa$_2$Co(PO$_4$)$_2$ [36] and spin-3/2 TLAs (K, Rb)Ag$_2$Cr(VO$_4$)$_2$ [34,37], piquing further interest in this series of compounds. Thus, this series of materials serves as a cradle for novel ground states where one can tune the ground state properties by changing the chemical pressure.

In the following, we delineate a comprehensive study of the thermodynamic properties of the frustrated spin-5/2 magnet Na$_3$Fe(PO$_4$)$_2$ in which the spins are embedded in a triangular lattice. It crystallizes in a monoclinic space group ($C2/c$) and belongs to the family $AA'M(XO_4)_2$ [38]. The crystal structure is presented in Fig. 1, where the slightly distorted FeO$_6$ octahedra are corner shared with distorted PO$_4$ tetrahedra in
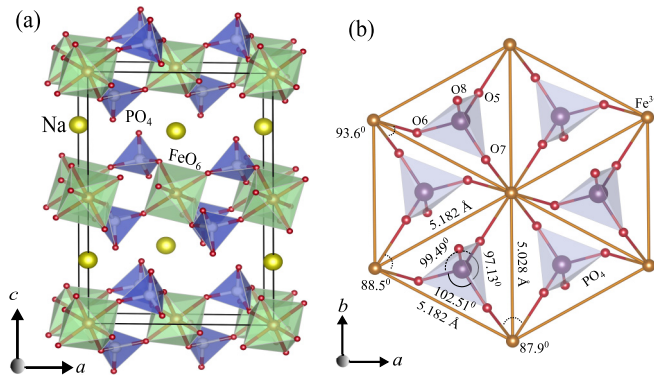
*rnath@iisertvm.ac.in

104425-1

FIG. 1. (a) Crystal structure of $Na_3Fe(PO_4)_2$ showing triangular layers sculpted by the corner-shared FeO_6 octahedra and PO_4 tetrahedra. Location of Na^+ ions is also shown. (b) A section of the layer showing Fe^{3+} ions linked via PO_4 tetrahedra on an anisotropic triangular lattice.

order to form the triangular Fe^{3+} ($3d^5$, spin-5/2) layers in the ab-plane which are stacked along the c-direction. Isolated Na atoms are found between the layers. In each layer, the Fe^{3+} triangles are slightly anisotropic with two Fe^{3+}-Fe^{3+} distances of 5.182 Å and one of 5.028 Å [Fig. 1(b)]. Further considering the analogy that the shortest Fe^{3+}-Fe^{3+} distance leads to a strong exchange interaction and the longer distance leads to a weak interaction, the spin lattice can also be viewed as coupled spin chains. Of course, the magnitude and sign of the interactions may vary depending on the actual path involved. Our magnetization data could be described well using the spin-5/2 isotropic triangle lattice model. It shows the onset of a magnetic ordering at $T_N \simeq 10.4$ K which is incisively detected to be a collinear AFM type. The $H - T$ phase diagram with a spin-flop (SF) transition confirms magnetic anisotropy in the compound.

II. METHODS

A polycrystalline sample of $Na_3Fe(PO_4)_2$ was synthesized following the conventional solid-state reaction technique. Prior to synthesis, the precursor $FePO_4$ was prepared by heating a stoichiometric mixture of Fe_2O_3 (Aldrich, 99.99%) and $(NH_4)_2HPO_4$ (Aldrich, 99.995%) at 880 °C for 12 h in air. In the next step, the raw materials Na_2CO_3 (Aldrich, 99.995%) and $(NH_4)_2HPO_4$ (Aldrich, 99.995%) were mixed with $FePO_4$ in stoichiometric ratios, grounded thoroughly, and pressed into pellets. The pellets were then sintered in an alumina crucible at 730 °C for three days in air with several intermediate grindings.

The phase purity of the sample was confirmed from the powder x-ray diffraction (XRD) performed at room temperature. For the powder XRD experiment, a PANalytical powder diffractometer with CuK_α radiation ($\lambda_{avg} \simeq 1.54182$ Å) was used. The temperature-dependent powder XRD measurement was performed over the temperature range 12.5 K ⩽ T ⩽ 300 K using a low-temperature attachment (Oxford Phenix) to the diffractometer. The dc magnetization (M) was measured on the powder sample using a superconducting quantum interference device (SQUID) (MPMS-3, Quantum Design) mag-

netometer. The measurements were performed in the temperature range 1.8 K ⩽ T ⩽ 380 K and in the magnetic field range 0 ⩽ H ⩽ 7 T. High-field magnetization was measured in a pulsed magnetic field at the Dresden high magnetic field laboratory. The details of the experimental procedure are described in Ref. [39]. Heat capacity as a function of temperature and magnetic field was measured on a small pellet using a Physical Property Measurement System (PPMS, Quantum Design).

Neutron powder diffraction (NPD) experiments were carried out in the temperature range 1.6 K ⩽ T ⩽ 15 K using the powder diffractometer (PD-II, $\lambda \simeq 1.2443$ Å) at Dhruva reactor, Bhabha Atomic Research Centre (BARC), Mumbai, India. The 1D neutron-depolarization measurements were performed using the polarized neutron spectrometer (PNS) at the Dhruva reactor, BARC, Mumbai ($\lambda \simeq 1.205$ Å). For this experiment, a polarized neutron beam was produced and analyzed using the magnetized Cu_2MnAl [reflection from (111) plane] and $Co_{0.92}Fe_{0.8}$ [reflection from (200) plane] single crystals, respectively. The two states of the polarization of the incident neutron beam were achieved by a flipper placed just before the sample. The flipping ratio (R) of the neutron beam was determined by measuring the intensities of neutrons in non-spin flip and spin flip channels with the flipper on and off, respectively. Rietveld refinement of the powder XRD and NPD data was performed using the FULLPROF software package [40].

Quantum Monte Carlo (QMC) simulation and full diagonalization were performed using the loop and fulldiag algorithms [41] of the ALPS package [42].

III. RESULTS

A. X-ray diffraction

In order to check the structural phase transition or lattice distortion, the sample was examined by measuring the XRD pattern at different temperatures. Figure 2 displays the powder XRD pattern at two end temperatures along with the Rietveld fits. The obtained lattice parameters from the refinement at room temperature are $a = 9.0714(2)$ Å, $b = 5.032(1)$ Å, $c = 13.8683(3)$ Å, and $\beta = 91.44(1)°$ and the unit cell volume $V_{cell} \simeq 632.96$ Å³, which are in close agreement with the previous report [38]. Temperature variation of the lattice constants (a, b, and c) and V_{cell} are shown in Fig. 3. All of them are found to decrease systematically upon cooling down to 12.5 K, as expected. No anomaly at the temperature corresponding to the magnetic transition suggests the absence of significant magnetoelastic coupling.

Such a temperature dependence of V_{cell} is usually described well by [43]

$$V(T) = \gamma U(T)/K_0 + V_0, \qquad (1)$$

where V_0 is the cell volume in the zero temperature limit, K_0 is the bulk modulus, and γ is the Grüneisen parameter. $U(T)$ is the internal energy, which can be derived in terms of the Debye approximation as

$$U(T) = 9nk_B T \left(\frac{T}{\theta_D}\right)^3 \int_0^{\theta_D/T} \frac{x^3}{e^x - 1} dx. \qquad (2)$$

Here, n is the number of atoms in the unit cell and k_B is the Boltzmann constant. As shown in Fig. 3(b), $V_{cell}(T)$ above
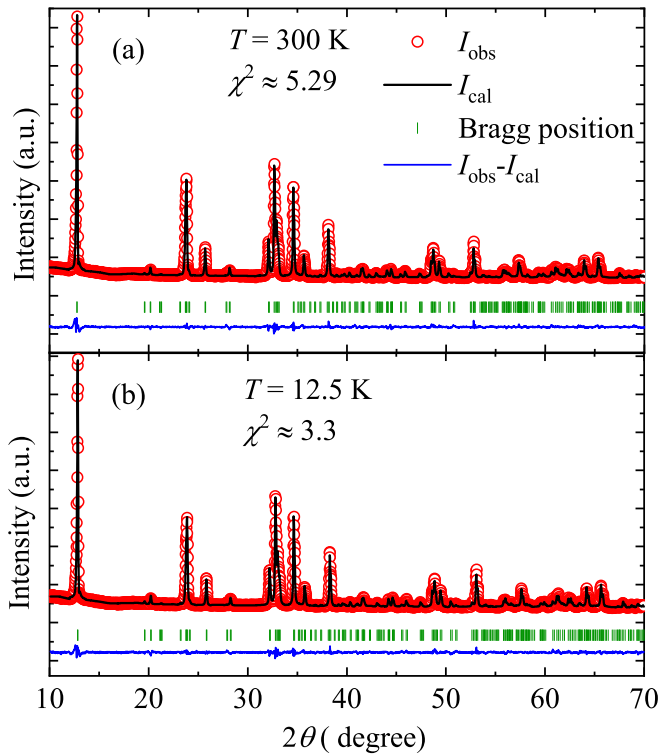
FIG. 2. Powder XRD pattern of $Na_3Fe(PO_4)_2$ measured at (a) $T = 300$ K and (b) $T = 12.5$ K. The open circles are the experimental data and the solid black line is the Rietveld refined fit. The Bragg positions are indicated by green vertical bars and the bottom solid blue line indicates the difference between the experimental and calculated intensities.
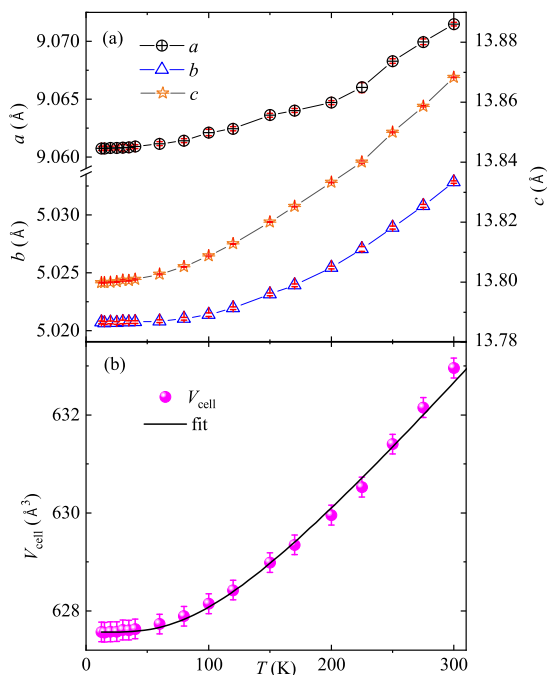

FIG. 3. (a) Lattice constants (a, b, and c) and (b) unit cell volume (V_{cell}) are plotted as a function of temperature from 12.5 to 300 K. The solid line in (b) represents the fit using Eq. (1).

12.5 K was fitted reasonably by Eq. (1) producing the parameters: Debye temperature $\theta_D \simeq 400$ K, $\gamma/K_0 \simeq 8.41 \times 10^{-5}$ P a^{-1}, and $V_0 \simeq 627.6$ Å^3.

B. Magnetization

Temperature-dependent magnetic susceptibility χ ($\equiv M/H$) of the polycrystalline $Na_3Fe(PO_4)_2$ sample measured in 0.5 T applied field is shown in Fig. 4(a). The most significant feature in $\chi(T)$ is the presence of a broad maximum at $T_\chi^{max} \simeq 15$ K, mimicking the AFM short-range order, typical for low-dimensional spin systems. While going further below this broad maxima, a change in slope is observed at $T_N \simeq 10.4$ K, which marks an alteration towards an AFM long-range order (LRO). The ordering temperature is very well evident in the $d\chi/dT$ vs T plot (not shown). To understand the nature of the magnetic ordering, $\chi(T)$ was measured at different applied fields up to 7 T [see the inset of Fig. 4(b)]. With increasing H, T_N remains unchanged up to 3 T and then moves weakly towards high temperatures above 3 T. For $H \geqslant 3$ T, $\chi(T)$ below T_N develops into a contort, which emphasizes that there is some field-induced spin canting prevailing in the system.

The zero-field-cooled (ZFC) and field-cooled (ZFC) susceptibilities as a function of temperature were measured in a low field of 0.01 T (not shown here). The absence of splitting between ZFC and FC $\chi(T)$s certainly rules out the possibility of any spin-glass transition or spin freezing at low temperatures.

For the purpose of analysis, $\chi(T)$ data in the high temperature regime were fitted using the Curie-Weiss (CW) law

$$\chi(T) = \chi_0 + \frac{C}{T + \theta_{CW}}, \tag{3}$$

where χ_0 is the temperature-independent susceptibility, C is the Curie constant, and θ_{CW} is the characteristic CW temperature. The fit shown in Fig. 4(b) for $T \geqslant 150$ K yields the parameters $\chi_0 \simeq -5.25 \times 10^{-4}$ cm^3/mol, $C \simeq 4.9906$ cm^{3}K/mol, and $\theta_{CW} \simeq 37.01$ K. A positive value of θ_{CW} indicates the presence of dominant AFM interactions between the Fe^{3+} ions. From the θ_{CW} and T_N values, we can quantify frustration by the frustration ratio, $f (= |\theta_{CW}/T_N|) \simeq 3.6$, which apprises us that the system is moderately frustrated. The core diamagnetic susceptibility χ_{core} of $Na_3Fe(PO_4)_2$ was calculated to be -1.23×10^{-4} cm^3/mol by summing the core diamagnetic susceptibilities of individual ions Na^+, Fe^{3+}, P^{5+}, and O^{2-} [44]. The Van Vleck paramagnetic susceptibility (χ_{VV}), which arises from the second-order contribution to free energy in the presence of magnetic field, was obtained by subtracting χ_{core} from χ_0 to be $\sim -4.03 \times 10^{-4}$ cm^3/mol. Further, from the value of Curie constant C, the effective moment is calculated using the relation $\mu_{eff} = \sqrt{3k_BC/N_A}$ to be $\mu_{eff} \simeq 6.319\mu_B$, where μ_B is the Bohr magneton and N_A is Avogadro's number. For a spin-5/2 system, the spin-only effective moment is expected to be $\mu_{eff} = g\sqrt{S(S+1)}\mu_B \simeq 5.916\mu_B$, assuming Landé g-factor $g = 2$. However, our experimental value of $\mu_{eff} \simeq 6.31\mu_B$ is slightly higher than the spin-only value and corresponds to $g \simeq 2.15$. This value of g is consistently reproduced from the spin model fit discussed later, suggesting a remnant orbital contribution. In the mean-
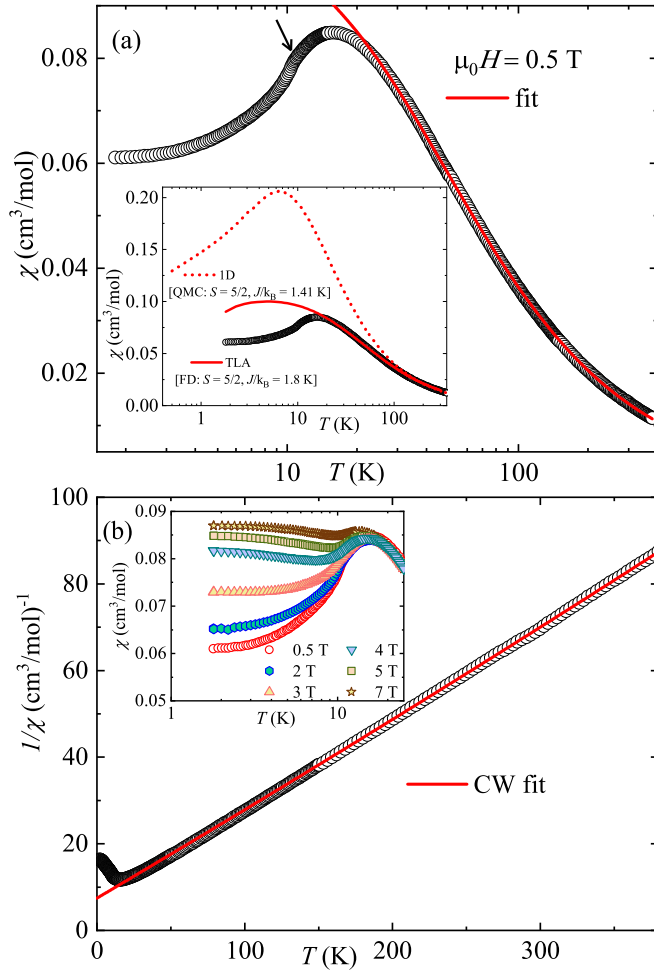
FIG. 4. (a) χ as a function of temperature in an applied field $\mu_0 H = 0.5$ T. The downward arrow points to the transition temperature (T_N). The solid line represents the fit using isotropic triangular lattice model [Eq. (4)]. Inset: comparison of experimental data with spin-5/2 uniform chain model and isotropic triangular lattice simulated using QMC and full diagonalization (FD), respectively. (b) Inverse susceptibility $1/\chi$ vs T and the solid line represents the CW fit, as discussed in the text. Inset: $\chi(T)$ measured in different fields, below T_N.
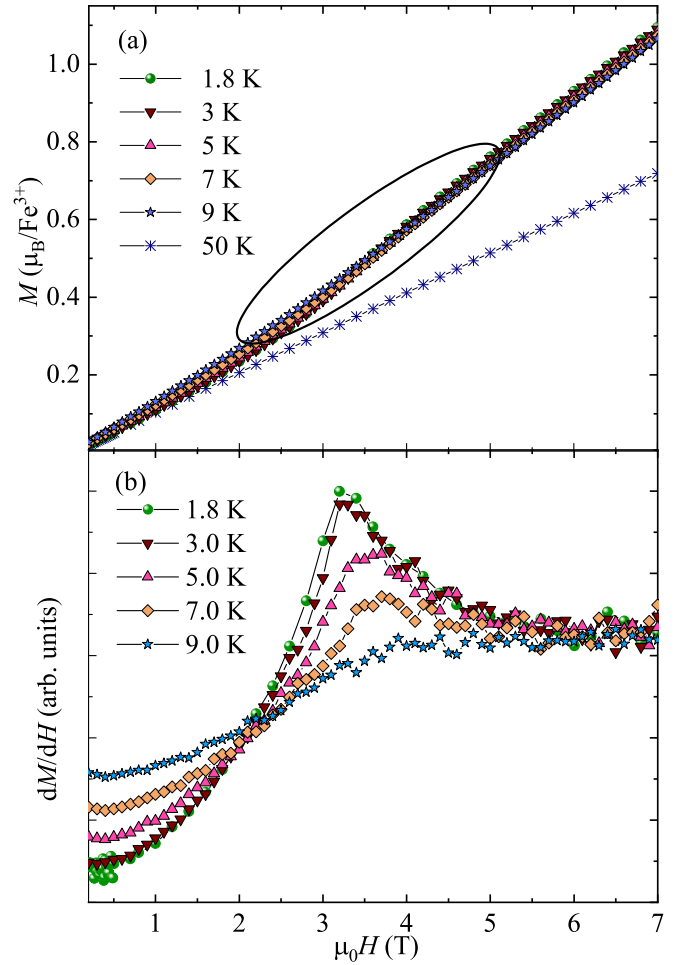

FIG. 5. (a) Magnetization (M) vs H measured at various temperatures from 1.8 K to 50 K. The encircled portion depicts the field induced transition regime. (b) The derivative dM/dH vs H is plotted at various temperatures from 1.8 K to 9 K in-order to highlight the field induced transition.

field approximation, θ_{CW} is a measure of energy scale of the total exchange interactions, which is related to the exchange coupling as $|\theta_{CW}| = \frac{JzS(S+1)}{3k_B}$, where $z = 6$ is the number of nearest neighbors of Fe^{3+} ions and J is the average intralayer exchange coupling [45]. In this way, we estimated the average exchange coupling within the triangular planes to be $J/k_B \simeq 2$ K.

Further, for a direct estimation of exchange coupling between the Fe^{3+} ions and to understand the spin lattice, we decomposed $\chi(T)$ into two components,

$$\chi(T) = \chi_0 + \chi_{spin}(T). \tag{4}$$

Here, $\chi_{spin}(T)$ typifies the intrinsic spin susceptibility which can be chosen according to the intrinsic magnetic model. As the Fe^{3+} ions in the crystal structure are arranged in triangles, we took the expression of the high temperature series expansion (HTSE) of χ_{spin} for a spin-5/2 Heisenberg isotropic TLA

model which has the form [46]

$$\frac{N_A \mu_B^2 g^2}{3|J|\chi_{spin}} = x + 4 + \frac{3.20}{x} - \frac{2.186}{x^2} + \frac{0.08}{x} + \frac{3.45}{x^4} - \frac{3.99}{x^5}, \tag{5}$$

with $x = k_B T/|J|S(S+1)$. This expression is valid for $T \geqslant JS(S+1)$ [47]. The solid line in Fig. 4(a) represents the best fit to the $\chi(T)$ data above 20 K by Eq. (4) resulting in $\chi_0 \simeq -6.22 \times 10^{-4}$ cm^3/mol, $g \simeq 2.11$, and the average AFM exchange coupling $J/k_B \simeq 1.8$ K. Indeed, this value of J/k_B is in good agreement with the value estimated from θ_{CW}. We also tried to fit the $\chi(T)$ data using HTSE for $\chi_{spin}(T)$ of the spin-5/2 Heisenberg 1D chain model in Eq. (4) [48]. The fit however did not converge giving unphysical parameters. Thus, the agreement of our experimental $\chi(T)$ data with the isotropic TLA model suggests frustrated triangular spin lattice in the system. To look for the field-induced transition, we measured the magnetization isotherms (M vs H) at different temperatures up to 7 T. As shown in Fig. 5(a), for $T < 10$ K a bend is observed in the intermediate magnetic fields which is the signature of a metastable field-induced transition. It
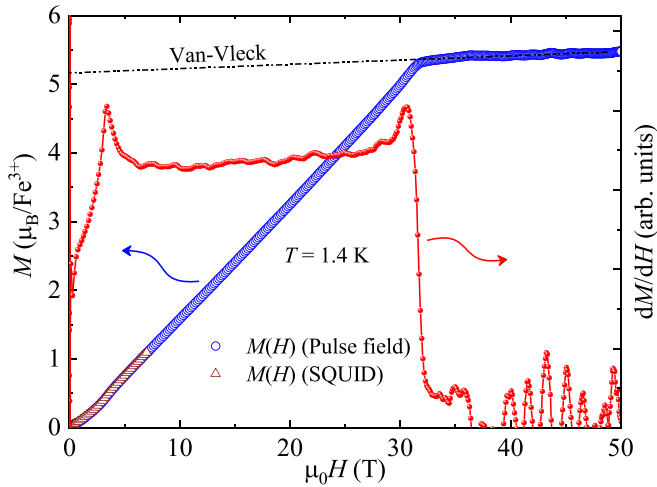
FIG. 6. Magnetization (M) and its field derivative dM/dH vs H measured at $T = 1.4$ K using pulsed magnetic field in the left and right y axes, respectively. The pulse field data are scaled with respect to the SQUID data measured up to 7 T. The dash-dotted line represents the saturation magnetization $M_{sat} \sim 5.2\mu_B$ per Fe^{3+} ion. The sharp peaks in dM/dH vs H plot depict the spin-flop and saturation fields $\mu_0 H_{SF} \simeq 3.2$ T and $\mu_0 H_{sat} \simeq 31.5$ T, respectively.

is more pronounced in the dM/dH vs H plots shown in Fig. 5(b), where this feature is manifested in a well defined peak. As the temperature rises, one can observe that the peak is moving slightly towards higher fields and then disappears completely for $T > 9$ K.

Further details about field induced transition and saturation magnetization can be obtained from the high field magnetization measurements. The M vs H data measured in a pulsed magnetic field up to 50 T at $T = 1.4$ K are plotted in Fig. 6. The pulse field magnetization curve is quantified by scaling it with respect to the SQUID data measured up to 7 T at $T = 1.8$ K. It exhibits a kink at $\mu_0 H_{SF} \simeq 3.2$ T, similar to that observed in Fig. 5, reminiscent of a spin-flop (SF) transition. Above H_{SF}, M increases almost linearly with H and develops a sharp bend towards saturation above $\mu_0 H_{sat} \simeq 31.5$ T. These two critical fields are very well visualized as sharp peaks in the dM/dH vs H plot. No obvious features associated with the 1/3 magnetization plateau are observed in the intermediate field range. In the polycrystalline sample, the random orientation of the grains with respect to the applied field direction might obscure this plateau. Above H_{sat}, M shows a slightly upward trend which may be due to a small Van-Vleck paramagnetic contribution. The linear interpolation of a straight line fit to the magnetization above H_{sat} intercepts the y-axis at $M_{sat} \sim 5.25\mu_B$. This saturation magnetization corresponds to the value expected for a spin-5/2 (Fe^{3+}) ion with $g = 2.1$. Further, in a spin system H_{sat} defines the energy required to overcome the AFM interactions and to polarize the spins in the direction of applied field. In particular, in a Heisenberg TLA, H_{sat} can be written in terms of the intralayer exchange coupling as $\mu_0 H_{sat} = 9JS/g\mu_B$ [49]. Our experimental value of $\mu_0 H_{sat} \simeq 31.5$ T yields an average exchange coupling of $J/k_B \simeq 1.95$ K, which is indeed close to the value obtained from the analysis of $\chi(T)$ and θ_{CW}. A small difference
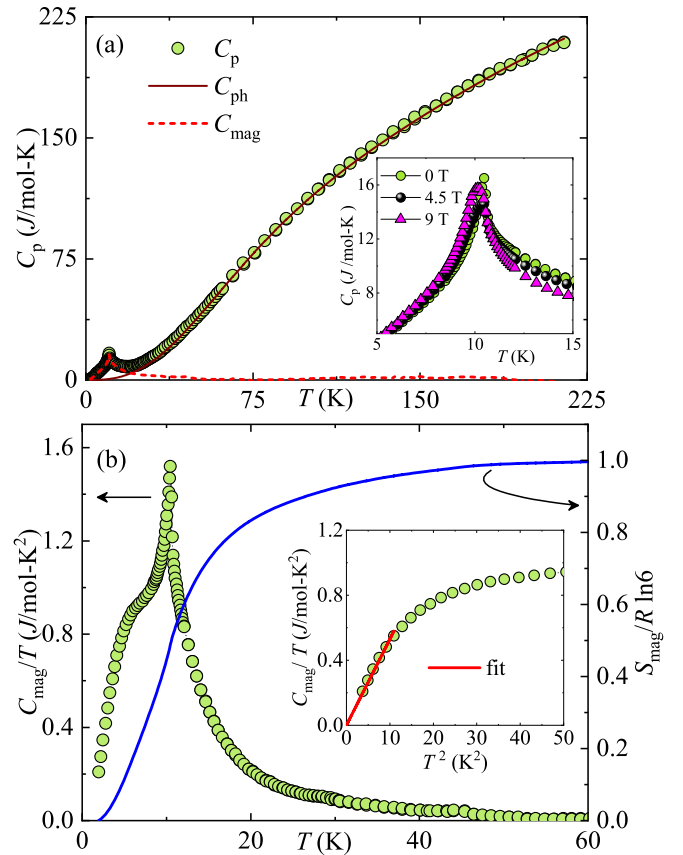

FIG. 7. (a) Heat capacity (C_p) as a function of temperature in zero applied field. The solid line represents the phonon contribution (C_{ph}) [Eq. (6)], while the dashed line indicates the magnetic contribution (C_{mag}). Inset: field dependence of $C_p(T)$ around T_N. (b) C_{mag}/T and S_{mag} vs T in the left and right y-axes, respectively. Inset: C_{mag}/T vs T^2 and the solid line is the linear fit.

can be attributed to the magnetic anisotropy present in the compound.

C. Heat capacity

The temperature-dependent heat capacity C_p of the polycrystalline sample measured in zero field is shown in Fig. 7(a). As we go lower in temperature, C_p also goes down systematically and then shows a pronounced λ-type anomaly at $T_N \simeq 10.4$ K, illustrating the crossover to a magnetically ordered state. Typically, in high temperatures, $C_p(T)$ in magnetic insulators has a dominant contribution from phonon excitations (C_{ph}), whereas, in low temperatures, the magnetic part of the heat capacity (C_{mag}) predominates over C_{ph}. Therefore, in magnetic systems with low energy scale of the exchange coupling, one can separate the magnetic part from the phononic part by analyzing C_p in the high temperature regime.

In order to demarcate C_{mag} from the total heat capacity C_p, the phonon contribution was first estimated by fitting the high-T data by a linear combination of one Debye and three Einstein terms [Debye-Einstein (DE) model] as [27,50]

$$C_{ph}(T) = f_D C_D(\theta_D, T) + \sum_{i=1}^{3} g_i C_{E_i}(\theta_{E_i}, T). \quad (6)$$

The first term in Eq. (6) represents the Debye model

$$C_D(\theta_D, T) = 9nR \left(\frac{T}{\theta_D}\right)^3 \int_0^{\frac{\theta_D}{T}} \frac{x^4 e^x}{(e^x - 1)^2} dx, \qquad (7)$$

where $x = \frac{\hbar \omega}{k_B T}$, ω is the frequency of oscillation, R is the universal gas constant, and θ_D is the characteristic Debye temperature. The flat optical modes in the phonon spectra are accounted for by the second term in Eq. (6), known as the Einstein term

$$C_E(\theta_E, T) = 3nR \left(\frac{\theta_E}{T}\right)^2 \frac{e^{\left(\frac{\theta_E}{T}\right)}}{[e^{\left(\frac{\theta_E}{T}\right)} - 1]^2}, \qquad (8)$$

where θ_E is the characteristic Einstein temperature. In Eq. (6) one can tentatively assign θ_D to the low-energy vibrations of the heavy atom (Fe) and the remaining three lighter atoms (Na, P, O) can be accounted for separately by the three Einstein terms, respectively. The coefficients f_D, g_1, g_2, and g_3 are the weight factors, which take into account the number of atoms per formula unit (n) and are chosen in such a way that at high temperatures the Dulong-Petit value ($\sim 3nR$) is satisfied [51].

The zero field $C_p(T)$ data above $\sim$20 K are fitted by Eq. (6) [see solid curve in Fig. 7(a)] and the obtained parameters are $f_D \simeq 0.075$, $g_1 \simeq 0.205$, $g_2 \simeq 0.30$, $g_3 \simeq 0.42$, $\theta_D \simeq 155$ K, $\theta_{E_1} \simeq 220$ K, $\theta_{E_2} \simeq 360$ K, and $\theta_{E_3} \simeq 930$ K. One may notice that the sum of f_D, g_1, g_2, and g_3 is close to one, as expected. Finally, the high-T fit was extrapolated down to 2 K and subtracted from $C_p(T)$ to get $C_{mag}(T)$ [see Fig. 7(a)]. Figure 7(b) presents $C_{mag}(T)/T$ and the corresponding magnetic entropy [$S_{mag}(T) = \int_{2\,K}^{T} \frac{C_{mag}(T')}{T'} dT'$] vs T. The obtained magnetic entropy which saturates above 50 K approaches a value $S_{mag} \simeq 14.85$ J/mol K and this value is close to the expected theoretical value $S_{mag} = R \ln(2S + 1) = 14.89$ J/mol K for a $S = 5/2$ system.

$C_P(T)$ measured in different applied fields in the low temperature regime is shown in the inset of Fig. 7(a). No noticeable shift in T_N is apparent for a field change from 0 to 9 T. Further, well below T_N, $C_{mag}(T)$ follows a T^3 behavior [inset of Fig. 7(b)], depicting the dominance of three-dimensional (3D) magnon excitations [24,52].

D. Neutron diffraction

The temperature evolution of the NPD pattern at different temperatures (1.6 to 15 K) is shown in Fig. 8. New peaks were found to appear below T_N at $Q \sim 0.6921$, 0.8180, 1.1227, 1.2503, and 1.5455 Å^{-1}. As we lower the temperature, the intensity of these peaks increases gradually, suggesting the emergence of magnetic reflections. The appearance of new magnetic reflections suggests the AFM nature of the transition [53]. In Fig. 8, the x-axis is shown in log scale in order to highlight these magnetic reflections in the low-Q (momentum transfer vector) regime. The magnetic peaks developed below T_N can be indexed with an ordering vector $k = (1, 0, 0)$, which insinuates a commensurate magnetic ordering. The Rietveld refinement of the nuclear pattern at $T = 15$ K was performed considering monoclinic crystal structure (space group: $C2/c$). The best fit of the data [see Fig. 9(a)] yields $a = 9.1085(2)$ Å, $b = 5.0532(1)$ Å, $c = 13.8733(3)$ Å, $\beta = 91.32(1)°$, and

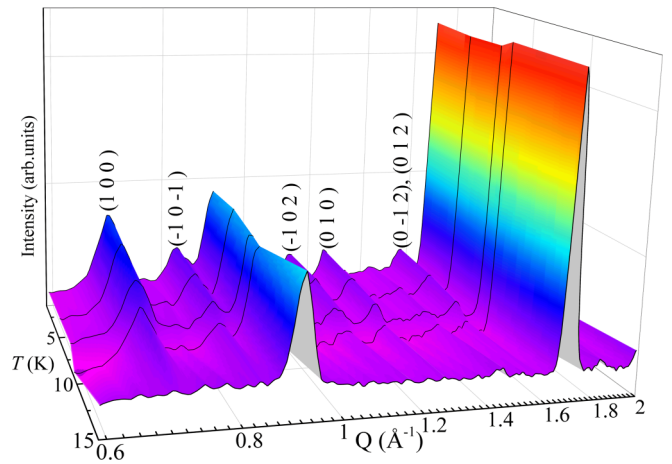

FIG. 8. Temperature evolution of the neutron powder diffraction (NPD) patterns of $Na_3Fe(PO_4)_2$ in the low-Q regime and for temperatures below 15 K. An emergence of magnetic reflections with $k = (1, 0, 0)$ is evident below T_N.

$V_{cell} \simeq 638.4$ Å^3. These obtained lattice parameters are in close agreement with the refined values from the powder XRD data at room temperature [38].

In the crystal structure of $Na_3Fe(PO_4)_2$, the magnetic Fe atom occupies $4a$ $(0, 0, 01)$ crystallographic site. For determining the magnetic structure the standard representational theory was used [54]. For the propagation vector $k = (1, 0, 0)$, the little group G_k can be generated using two symmetry
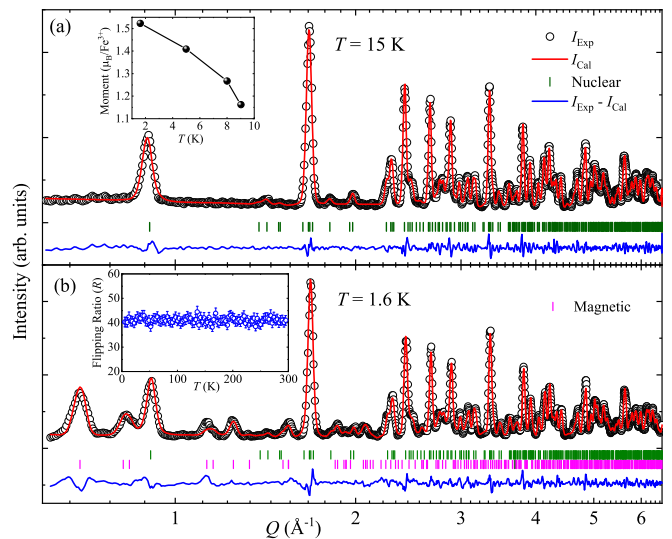

FIG. 9. Rietveld refinement of the neutron powder diffraction data at (a) $T = 15$ K and (b) $T = 1.6$ K, considering only nuclear reflections and nuclear + magnetic reflections, respectively. The experimental data are depicted as open black circles. The red solid line represents the calculated pattern. The difference in intensities of experimental and calculated data is shown as a blue solid line at the bottom. The allowed Bragg peaks corresponding to the nuclear (green) and magnetic (pink) reflections are shown as vertical bars. Inset of (a) represents the temperature variation of ordered magnetic moment, below T_N. Inset of (b) represents the variation of flipping ratio (R) in the T range 5 K $\leqslant T \leqslant$ 300 K.

TABLE I. Irreducible representations and basis vectors for the space group $C2/c$ with propagation vector $k = (1, 0, 0)$, obtained using the BasIreps software. The atoms are defined according to Fe1: $(0, 0, 0)$ and Fe2: $(0, 0, 0.5)$.

	Basis vector components for $k = (1, 0, 0)$		
IR	Basis vectors	Fe1	Fe2
Γ_1	Ψ_1	(1 0 0)	(−1 0 0)
	Ψ_2	(0 1 0)	(0 1 0)
	Ψ_3	(0 0 1)	(0 0 −1)
Γ_3	Ψ_4	(1 0 0)	(1 0 0)
	Ψ_5	(0 1 0)	(0 −1 0)
	Ψ_6	(0 0 1)	(0 0 1)

elements, $-x, y, -z + 1/2$ and $-x, -y, -z$. Our symmetry analysis shows that the magnetic representation for $4a$ site can be written in terms of the irreducible representations (IR) as $\Gamma(4a) = 3\Gamma_1^{(1)} + 3\Gamma_3^{(1)}$. Here, both IRs ($\Gamma_1$ and Γ_3) are one dimensional and are composed of basis vectors $\Psi_{1,2,3}$ and $\Psi_{4,5,6}$, respectively (see Table I).

The observed NPD patterns cannot be fitted with the magnetic structure corresponding to the representations Γ_1, whereas the magnetic structure corresponding to the representation Γ_3 is found to be appropriate to describe the observed NPD patterns. The magnetic structure belonging to the representation Γ_3 corresponds to an antiferromagnetic structure, where moments are aligned in the bc-plane with the dominant component along the crystallographic c-axis (Fig. 10). Further details of the spin structure are discussed in the next section. From the magnetic structure refinement, we were able to quantify the magnetic moment values along different crystalographic directions. At the lowest temperature ($T = 1.6$ K), these values are $\mu_b \simeq 0.83\mu_B$ and $\mu_c \simeq 1.27\mu_B$ along the b and c directions, respectively. The temperature variation of total moment ($\mu = \sqrt{\mu_b^2 + \mu_c^2}$) is shown in the inset of Fig. 9(a). The observed reduced value of the ordered moment with respect to the theoretically expected classical value of $5\mu_B$ for spin-5/2 could be attributed to the effect of low dimensionality and magnetic frustration and/or the presence of the covalence effect [33,55].

Further, to check the presence of any ferromagnetic-type correlations, we have also carried out the neutron depolarization measurements. The absence of depolarization is apparent from the flipping ratio (R) vs T plot, where R is found to be constant over the entire temperature range (5 K $\leqslant T \leqslant$ 300 K) [see the inset of Fig. 9(b)]. This rules out the possibility of any ferromagnetic-type correlations or spin canting in the system.

IV. DISCUSSION AND SUMMARY

Theoretically, for a spin-5/2 chain system, the broad maxima in $\chi(T)$ is expected at $k_B T_\chi^{max}/J = 10.6$ [56]. The broad maximum in our experimental data appears at $T_\chi^{max} \simeq 15$ K, which corresponds to the intrachain coupling of $J/k_B \simeq 1.41$ K. In order to reproduce the overall shape of the $\chi(T)$ plot, we simulated the data using the QMC technique, assuming a spin-chain model with $S = 5/2$ and $J/k_B \simeq 1.41$ K. As depicted in the inset of Fig. 4(a), the simulated data show a significant deviation from the experimental data, discarding the possibility of spin-chain physics. On the other hand, the fit assuming the isotropic triangular lattice [Eq. (4)] reproduces the experimental $\chi(T)$ data very well in the high temperature regime, despite a small spatial anisotropy. As a further test for the isotropic TLA model, we performed the full diagonalization for a spin-5/2 isotropic TLA with $J/k_B \simeq 1.8$ K [obtained from the $\chi(T)$ analysis]. As evident from the inset of Fig. 4(a), the simulated data using full diagonalization superimpose the experimental data above T_χ^{max}. This confirms that the spin lattice in $Na_3Fe(PO_4)_2$ behaves as more of a 2D triangular lattice rather than a 1D spin chain.

This compound orders antiferromagnetically below $T_N \simeq$ 10.4 K, which is clear from the appearance of magnetic reflections in the NPD pattern, λ-type anomaly in $C_p(T)$, and slope change in $\chi(T)$. The magnetic structure refined from the NPD data is shown in Fig. 10, which demonstrates a collinear AFM ordering. The spins are coupled ferromagnetically (J_1) along the b-axis or in the [100] plane, which is the direction of the shortest Fe^{3+}-Fe^{3+} distance. The AFM interchain coupling (J_2) ties the chains into a 2D anisotropic triangular layer in the ab-plane. Alternatively, one can visualize it as AFM cross chains running along the [110] and [−110] directions, which are coupled ferromagetically in the ab-plane. Though a non collinear 120° structure is understood as a hallmark of TLA, some compounds tend to deviate from this spin structure either due to anisotropy or interlayer coupling [57].

The crystal symmetry plays a key role in deciding the ground states of the compounds in the $AA'M(XO_4)_2$ family. The correspondence between crystal symmetry and exchange couplings is well demonstrated for the series $AAg_2Cr(VO_4)_2$ ($A =$ Ag, K, Rb) [37]. Here, replacement of A site induces a symmetry change in the CrO_6 octahedra. Therefore, $Ag_3Cr(VO_4)_2$ (space group: $C2/c$) is a distorted/anisotropic TLA with a collinear AFM ordering below $T_N \simeq 10$ K, whereas the other compounds ($A =$ K, Rb) with higher symmetry (space group: $P\bar{3}$) are undistorted/isotropic TLAs and are reported to show signature of QSL [37]. Several other compounds with higher symmetry in this series also feature
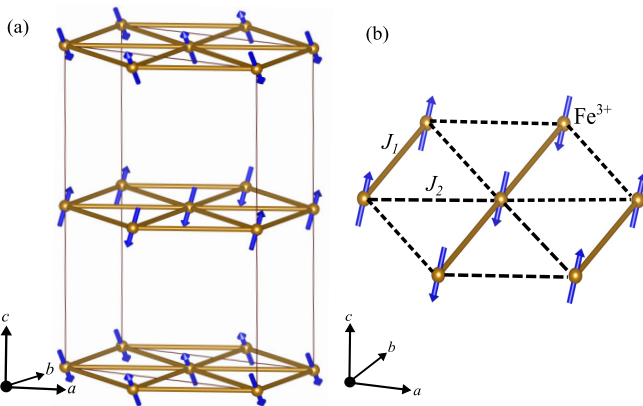

FIG. 10. (a) Spin structure of $Na_3Fe(PO_4)_2$ derived from the neutron powder diffraction at $T = 1.6$ K. (b) A section of the triangular layer (ab-plane) showing the spin orientation and exchange interactions.

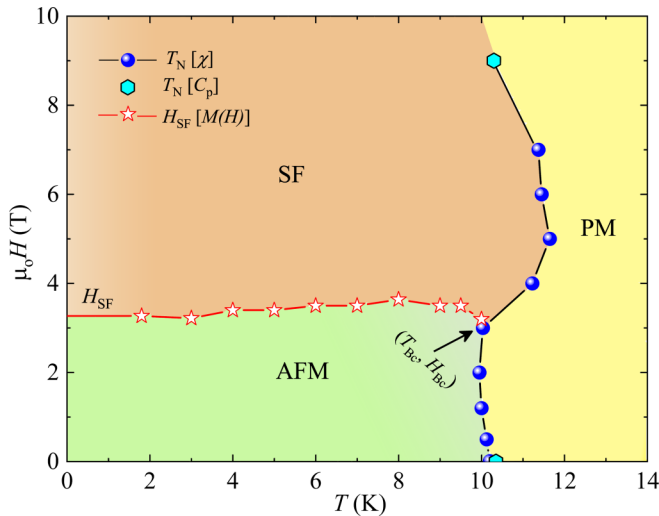FIG. 11. $H-T$ phase diagram of $Na_3Fe(PO_4)_2$ drawn from the magnetic isotherm, $\chi(T)$, and $C_p(T)$ measurements. H_{SF} represents the critical field at which the SF transition takes place. The point (T_{Bc}, H_{Bc}) denotes the bicritical point, where the SF transition ends.

isotropic triangular lattices [29,33,34,37,58]. As pointed out in Fig. 1(b), for $Na_3Fe(PO_4)_2$, the PO_4 tetrahedra which acts as a medium of interaction among the Fe^{3+} ions is distorted where the P-O bond distance varies from 1.50 Å to 1.56 Å and the $\angle O-P-O$ angles are also different. These give rise to nonequivalent exchange interactions along the edges of the triangle. The anisotropic interactions can also be assessed from the deviation of O-Fe-O bond angles from $90°$, typically expected for an isotropic triangular lattice formed by undistorted FeO_6 octahedra. It is also to be noted that, despite the shortest Fe^{3+}-Fe^{3+} distance, the interaction along the [100] direction is FM. A close inspection of the bond angles reveals that $\angle O-P-O$ along the [100] direction has the smallest value of $97.13°$ compared to the other directions which possibly favor parallel alignment. The collinear order in $Na_3Fe(PO_4)_2$ may thus be attributed to the distortion in FeO_6 octahedra and interlayer coupling along the stacking c direction, similar to $Ag_3Cr(VO_4)_2$.

The obtained T_N from $\chi(T)$ and $C_p(T)$ data and the critical field (H_{SF}) corresponding to the metastable transition obtained from the magnetic isotherms are summarized in Fig. 11 as an $H-T$ phase diagram. It displays three well defined regions represented as paramagnetic (PM), antiferromagnetic (AFM), and spin-flop (SF) phases. The

majority of TLAs feature a magnetization plateau at 1/3 of the saturation magnetization in the magnetic isotherms [59–62], where the system evolves from a $120°$ AFM order, which is the true ground state of a Heisenberg TLA [5] to an up-up-down (*uud*) phase. The *uud* phase is stabilized by the magnetic field that introduces axial (Ising) anisotropy and disfavors the noncollinear $120°$ order. Though our low temperature isotherms illustrate a plateau, it is well below the 1/3 of the saturation magnetization [63]. Further, the magnetic ordering in zero field is a collinear AFM order rather than a noncollinear $120°$ order. Hence, the 1/3 magnetization plateau is overruled. Moreover, the presence of an easy-plane (*XY*-type) anisotropy often triggers field emergent phenomenon like a SF transition [64] above a critical field H_{SF}, where the moments flip from parallel to perpendicular direction with respect to the applied field. Thus, the metastable/SF transition in $Na_3Fe(PO_4)_2$ can be attributed to the easy-plane anisotropy in the compound. $Na_2BaMnV_2O_8$, which belongs to the same series, also shows a SF transition at low temperatures [31]. A similar phase diagram is also reported previously in the frustrated spin chain compounds $SrCuTe_2O_6$ and α-$Cu_2As_2O_7$ [65].

In summary, we have demonstrated the ground state properties of the frustrated magnet $Na_3Fe(PO_4)_2$. Based on the structural data one may anticipate a small anisotropy in the exchange couplings in the triangular unit. However, the analysis of our experimental data emphasizes that the system behaves more like a spin-5/2 isotropic triangular lattice. It stabilizes in a collinear antiferromagnetic ordering below T_N likely due to moderate interlayer coupling. The occurrence of a field induced SF transition in the low temperature magnetic isotherms insinuates the presence of XY-type anisotropy. A comparison with other members of the $AA'M(XO_4)_2$ family reveals that the bond distances between metal ions and the corresponding angles become more anisotropic with reduced symmetry, leading to a potential structural complexity and exotic ground states.

[1] M. F. Collins and O. A. Petrenko, Review/Synthèse: Triangular antiferromagnets, Can. J. Phys. **75**, 605 (1997); O. A. Starykh, Unusual ordered phases of highly frustrated magnets: A review, Rep. Prog. Phys. **78**, 052502 (2015).

[2] L. Balents, Spin liquids in frustrated magnets, Nature (London) **464**, 199 (2010).

[3] T. Jolicoeur and J. C. Le Guillou, Spin-wave results for the triangular Heisenberg antiferromagnet, Phys. Rev. B **40**, 2727 (1989).

[4] A. V. Chubukov, S. Sachdev, and T. Senthil, Large-S expansion for quantum antiferromagnets on a triangular lattice, J. Phys.: Condens. Matter **6**, 8891 (1994).

[5] L. Capriotti, A. E. Trumper, and S. Sorella, Long-Range Néel Order in the Triangular Heisenberg Model, Phys. Rev. Lett. **82**, 3899 (1999).

[6] B. Bernu, P. Lecheminant, C. Lhuillier, and L. Pierre, Exact spectra, spin susceptibilities, and order parameter of the quantum Heisenberg antiferromagnet on the triangular lattice, Phys. Rev. B **50**, 10048 (1994).

[7] A. L. Chernyshev and M. E. Zhitomirsky, Spin waves in a triangular lattice antiferromagnet: Decays, spectrum renormalization, and singularities, Phys. Rev. B **79**, 144416 (2009).

[8] H. Kawamura and S. Miyashita, Phase transition of the two-dimensional heisenberg antiferromagnet on the triangular lattice, J. Phys. Soc. Jpn. **53**, 4138 (1984).

[9] S. Miyashita and H. Kawamura, Phase transitions of anisotropic Heisenberg antiferromagnets on the triangular lattice, J. Phys. Soc. Jpn. **54**, 3385 (1985).

[10] P.-E. Melchy and M. E. Zhitomirsky, Interplay of anisotropy and frustration: Triple transitions in a triangular-lattice antiferromagnet, Phys. Rev. B **80**, 064411 (2009).

[11] R. H. Clark and W. G. Moulton, Cs^{133} and Cl^{35} NMR in antiferromagnetic $CsNiCl_3$, Phys. Rev. B **5**, 788 (1972).

[12] H. Kadowaki, K. Ubukoshi, and K. Hirakawa, Neutron scattering study of successive phase transitions in triangular lattice antiferromagnet $CsNiCl_3$, J. Phys. Soc. Jpn. **56**, 751 (1987).

[13] Y. Ajiro, T. Inami, and H. Kadowaki, Magnetic phase transition of the triangular lattice antiferromagnet $CsMnI_3$, J. Phys. Soc. Jpn. **59**, 4142 (1990).

[14] A. Harrison, M. F. Collins, J. Abu-Dayyeh, and C. V. Stager, Magnetic structures and excitations of $CsMnI_3$: A one-dimensional Heisenberg antiferromagnet with easy-axis anisotropy, Phys. Rev. B **43**, 679 (1991).

[15] K. M. Ranjith, K. Brinda, U. Arjun, N. G. Hegde, and R. Nath, Double phase transition in the triangular antiferromagnet $Ba_3CoTa_2O_9$, J. Phys.: Condens. Matter **29**, 115804 (2017);

[16] M. Lee, E. S. Choi, X. Huang, J. Ma, C. R. Dela Cruz, M. Matsuda, W. Tian, Z. L. Dun, S. Dong, and H. D. Zhou, Magnetic phase diagram and multiferroicity of $Ba_3MnNb_2O_9$: A spin-$\frac{5}{2}$ triangular lattice antiferromagnet with weak easy-axis anisotropy, Phys. Rev. B **90**, 224402 (2014). M. Lee, J. Hwang, E. S. Choi, J. Ma, C. R. Dela Cruz, M. Zhu, X. Ke, Z. L. Dun, and H. D. Zhou, Series of phase transitions and multiferroicity in the quasi-two-dimensional spin-$\frac{1}{2}$ triangular-lattice antiferromagnet $Ba_3CoNb_2O_9$, *ibid.* **89**, 104420 (2014).

[17] Z. Lu, L. Ge, G. Wang, M. Russina, G. Günther, C. R. dela Cruz, R. Sinclair, H. D. Zhou, and J. Ma, Lattice distortion effects on the frustrated spin-1 triangular-antiferromagnet $A_3NiNb_2O_9$ (A = Ba, Sr, and Ca), Phys. Rev. B **98**, 094412 (2018); R. Rawl, M. Lee, E. S. Choi, G. Li, K. W. Chen, R. Baumbach, C. R. dela Cruz, J. Ma, and H. D. Zhou, Magnetic properties of the triangular lattice magnets $A_4B'B_2O_{12}$ (A = Ba, Sr, La; B' = Co, Ni, Mn; B = W, Re), *ibid.* **95**, 174438 (2017).

[18] S. Miyashita, Magnetic properties of Ising-like Heisenberg antiferromagnets on the triangular lattice, J. Phys. Soc. Jpn. **55**, 3605 (1986).

[19] R. Rawl, L. Ge, Z. Lu, Z. Evenson, C. R. dela Cruz, Q. Huang, M. Lee, E. S. Choi, M. Mourigal, H. D. Zhou, and J. Ma, $Ba_8MnNb_6O_{24}$: A model two-dimensional spin-$\frac{5}{2}$ triangular lattice antiferromagnet, Phys. Rev. Mater. **3**, 054412 (2019).

[20] S.-W. Cheong and M. Mostovoy, Multiferroics: A magnetic twist for ferroelectricity, Nat. Mater. **6**, 13 (2007).

[21] Z. Zhu, P. A. Maksimov, S. R. White, and A. L. Chernyshev, Disorder-Induced Mimicry of a Spin Liquid in $YbMgGaO_4$, Phys. Rev. Lett. **119**, 157201 (2017).

[22] Z. Zhu, P. A. Maksimov, S. R. White, and A. L. Chernyshev, Topography of Spin Liquids on a Triangular Lattice, Phys. Rev. Lett. **120**, 207203 (2018).

[23] D. Heidarian, S. Sorella, and F. Becca, Spin-$\frac{1}{2}$ Heisenberg model on the anisotropic triangular lattice: From magnetism to a one-dimensional spin liquid, Phys. Rev. B **80**, 012404 (2009).

[24] K. Somesh, Y. Furukawa, G. Simutis, F. Bert, M. Prinz-Zwick, N. Büttgen, A. Zorko, A. A. Tsirlin, P. Mendels, and R. Nath, Universal fluctuating regime in triangular chromate antiferromagnets, Phys. Rev. B **104**, 104422 (2021).

[25] D. Yamamoto, T. Sakurai, R. Okuto, S. Okubo, H. Ohta, H. Tanaka, and Y. Uwatoko, Continuous control of classical-quantum crossover by external high pressure in the coupled chain compound $CsCuCl_3$, Nat. Commun. **12**, 4263 (2021).

[26] K. M. Ranjith, R. Nath, M. Majumder, D. Kasinathan, M. Skoulatos, L. Keller, Y. Skourski, M. Baenitz, and A. A. Tsirlin, Commensurate and incommensurate magnetic order in spin-1 chains stacked on the triangular lattice in $Li_2NiW_2O_8$, Phys. Rev. B **94**, 014415 (2016).

[27] S. J. Sebastian, K. Somesh, M. Nandi, N. Ahmed, P. Bag, M. Baenitz, B. Koo, J. Sichelschmidt, A. A. Tsirlin, Y. Furukawa, and R. Nath, Quasi-one-dimensional magnetism in the spin-$\frac{1}{2}$ antiferromagnet $BaNa_2Cu(VO_4)_2$, Phys. Rev. B **103**, 064413 (2021).

[28] N. E. Amuneke, D. E. Gheorghe, B. Lorenz, and A. Möller, Synthesis, crystal structure, and physical properties of $BaAg_2Cu[VO_4]_2$: A new member of the $S = 1/2$ triangular lattice, Inorg. Chem. **50**, 2207 (2011).

[29] N. E. Amuneke, J. Tapp, C. R. dela Cruz, and A. Möller, Experimental realization of a unique class of compounds: XY-antiferromagnetic triangular lattices, $KAg_2Fe[VO_4]_2$ and $RbAg_2Fe[VO_4]_2$, with ferroelectric ground states, Chem. Mater. **26**, 5930 (2014).

[30] A. Möller, N. E. Amuneke, P. Daniel, B. Lorenz, C. R. dela Cruz, M. Gooch, and P. C. W. Chu, $AAg_2M[VO_4]_2$ (A = Ba, Sr; M = Co, Ni): A series of ferromagnetic insulators, Phys. Rev. B **85**, 214422 (2012).

[31] G. Nakayama, S. Hara, H. Sato, Y. Narumi, and H. Nojiri, Synthesis and magnetic properties of a new series of triangular-lattice magnets, $Na_2BaMV_2O_8$(M = Ni, Co, and Mn), J. Phys.: Condens. Matter **25**, 116003 (2013).

[32] A. Reuß, V. Ksenofontov, J. Tapp, D. Wulferding, P. Lemmens, M. Panthöfer, and A. Möller, Screw-type motion and its impact on cooperativity in $BaNa_2Fe[VO_4]_2$, Inorg. Chem. **57**, 6300 (2018).

[33] L. D. Sanjeewa, V. O. Garlea, M. A. McGuire, C. D. McMillen, and J. W. Kolis, Magnetic ground state crossover in a series of glaserite systems with triangular magnetic lattices, Inorg. Chem. **58**, 2813 (2019).

[34] S. Lee, R. Klauer, J. Menten, W. Lee, S. Yoon, H. Luetkens, P. Lemmens, A. Möller, and K.-Y. Choi, Unconventional spin excitations in the $S = \frac{3}{2}$ triangular antiferromagnet $RbAg_2Cr[VO_4]_2$, Phys. Rev. B **101**, 224420 (2020).

[35] A. A. Tsirlin, A. Möller, B. Lorenz, Y. Skourski, and H. Rosner, Superposition of ferromagnetic and antiferromagnetic spin chains in the quantum magnet $BaAg_2Cu[VO_4]_2$, Phys. Rev. B **85**, 014401 (2012).

[36] S. Lee, C. H. Lee, A. Berlie, A. D. Hillier, D. T. Adroja, R. Zhong, R. J. Cava, Z. H. Jang, and K.-Y. Choi, Temporal and field evolution of spin excitations in the disorder-free triangular antiferromagnet $Na_2BaCo(PO_4)_2$, Phys. Rev. B **103**, 024413 (2021).

[37] J. Tapp, C. R. dela Cruz, M. Bratsch, N. E. Amuneke, L. Postulka, B. Wolf, M. Lang, H. O. Jeschke, R. Valentí, P. Lemmens, and A. Möller, From magnetic order to spin-liquid ground states on the $S = \frac{3}{2}$ triangular lattice, Phys. Rev. B **96**, 064404 (2017).

[38] V. Morozov, B. Lazoryak, A. Malakho, K. Pokholok, S. Polyakov, and T. Terekhina, The glaserite-like structure of double sodium and iron phosphate $Na_3Fe(PO_4)_2$, J. Solid State Chem. **160**, 377 (2001); M. Belkhiria, S. Laaribi, A. Ben Hadj Amara, and M. Ben Amara, Structure of $Na_3Fe(PO_4)_2$ from powder X-ray data, Ann. Chim.: Sci. Mater. **23**, 117 (1998).

[39] Y. Skourski, M. D. Kuz'min, K. P. Skokov, A. V. Andreev, and J. Wosnitza, High-field magnetization of Ho_2Fe_{17}, Phys. Rev. B **83**, 214420 (2011); A. A. Tsirlin, B. Schmidt, Y. Skourski, R. Nath, C. Geibel, and H. Rosner, Exploring the spin-$\frac{1}{2}$ frustrated square lattice model with high-field magnetization studies, *ibid.* **80**, 132407 (2009).

[40] J. Rodríguez-Carvajal, Recent advances in magnetic structure determination by neutron powder diffraction, Phys. B: Condens. Matter **192**, 55 (1993).

[41] S. Todo and K. Kato, Cluster Algorithms for General-S Quantum Spin Systems, Phys. Rev. Lett. **87**, 047203 (2001).

[42] A. Albuquerque, F. Alet, P. Corboz, P. Dayal, A. Feiguin, S. Fuchs, L. Gamper, E. Gull, S. Gürtler, A. Honecker, R. Igarashi, M. Körner, A. Kozhevnikov, A. Läuchli, S. Manmana, M. Matsumoto, I. McCulloch, F. Michel, R. Noack, G. Pawłowski *et al.*, The alps project release 1.3: Open-source software for strongly correlated systems, J. Magn. Magn. Mater. **310**, 1187 (2007).

[43] S. S. Islam, K. M. Ranjith, M. Baenitz, Y. Skourski, A. A. Tsirlin, and R. Nath, Frustration of square cupola in $Sr(TiO)Cu_4(PO_4)_4$, Phys. Rev. B **97**, 174432 (2018).

[44] P. W. Selwood, *Magnetochemistry* (Read Books Ltd., Redditch, Worcestershire, 2013); L. B. Mendelsohn, F. Biggs, and J. B. Mann, Hartree-Fock diamagnetic susceptibilities, Phys. Rev. A **2**, 1130 (1970).

[45] C. Domb and A. Miedema, Chapter VI magnetic transitions, J. Low Temp. Phys. **4**, 296 (1964).

[46] C. Delmas, G. Le Flem, C. Fouassier, and P. Hagenmuller, Etude comparative des proprietes magnetiques des oxydes lamellaires $ACrO_2$ ($A =$ Li, Na, K)'II: Calcul des integrales d'echange, J. Phys. Chem. Solids **39**, 55 (1978).

[47] H. J. Schmidt, A. Lohmann, and J. Richter, Eighth-order high-temperature expansion for general Heisenberg Hamiltonians, Phys. Rev. B **84**, 104443 (2011).

[48] R. Dingle, M. E. Lines, and S. L. Holt, Linear-chain antiferromagnetism in $[(CH_3)_4N][MnCl_3]$, Phys. Rev. **187**, 643 (1969).

[49] H. Kawamura and S. Miyashita, Phase transition of the Heisenberg antiferromagnet on the triangular lattice in a magnetic field, J. Phys. Soc. Jpn. **54**, 4530 (1985).

[50] E. S. R. Gopal, *Specific Heats at Low Temperatures* (Springer Science & Business Media, New York, 2012).

[51] R. K. Fitzgerel and F. H. Verhoek, The law of dulong and petit, J. Chem. Educ. **37**, 545 (1960).

[52] P. Bag, N. Ahmed, V. Singh, M. Sahoo, A. A. Tsirlin, and R. Nath, Low-dimensional magnetism of $BaCuTe_2O_6$, Phys. Rev. B **103**, 134410 (2021);

[53] V. K. Anand, L. Opherden, J. Xu, D. T. Adroja, A. D. Hillier, P. K. Biswas, T. Herrmannsdörfer, M. Uhlarz, J. Hornung, J. Wosnitza, E. Canévet, and B. Lake, Evidence for a dynamical

ground state in the frustrated pyrohafnate $Tb_2Hf_2O_7$, Phys. Rev. B **97**, 094402 (2018). S. S. Islam, V. Singh, K. Somesh, P. K. Mukharjee, A. Jain, S. M. Yusuf, and R. Nath, Unconventional superparamagnetic behavior in the modified cubic spinel compound $LiNi_{0.5}Mn_{1.5}O_4$, *ibid.* **102**, 134433 (2020).

[54] E. Bertaut, *Spin Configurations of Ionic Structures: Theory and Practice*, Magnetism (edited by G. T. Rado and H. Shul) 3, 149 (1963).

[55] P. Saeaun, Y. Zhao, P. Piyawongwatthana, T. J. Sato, F. C. Chou, M. Avdeev, G. Gitgeatpong, and K. Matan, Magnetic properties and magnetic structure of the frustrated quasi-one-dimensional antiferromagnet $SrCuTe_2O_6$, Phys. Rev. B **102**, 134407 (2020).

[56] L. J. D. Jongh and A. R. Miedema, Experiments on simple magnetic model systems, Adv. Phys. **50**, 947 (2001);

[57] K. M. Ranjith, R. Nath, M. Skoulatos, L. Keller, D. Kasinathan, Y. Skourski, and A. A. Tsirlin, Collinear order in the frustrated three-dimensional spin-$\frac{1}{2}$ antiferromagnet $Li_2CuW_2O_8$, Phys. Rev. B **92**, 094426 (2015); K. M. Ranjith, M. Majumder, M. Baenitz, A. A. Tsirlin, and R. Nath, Frustrated three-dimensional antiferromagnet $Li_2CuW_2O_8$: ^7Li NMR and the effect of nonmagnetic dilution, *ibid.* **92**, 024422 (2015).

[58] C. Wellm, W. Roscher, J. Zeisner, A. Alfonsov, R. Zhong, R. J. Cava, A. Savoyant, R. Hayn, J. van den Brink, B. Büchner, O. Janson, and V. Kataev, Frustration enhanced by Kitaev exchange in a $\tilde{j}_{\mathrm{eff}} = \frac{1}{2}$ triangular antiferromagnet, Phys. Rev. B **104**, L100420 (2021).

[59] A. V. Chubukov and D. I. Golosov, Quantum theory of an antiferromagnet on a triangular lattice in a magnetic field, J. Phys.: Condens. Matter **3**, 69 (1991).

[60] T. Ono, H. Tanaka, H. Aruga Katori, F. Ishikawa, H. Mitamura, and T. Goto, Magnetization plateau in the frustrated quantum spin system Cs_2CuBr_4, Phys. Rev. B **67**, 104431 (2003); T. Susuki, N. Kurita, T. Tanaka, H. Nojiri, A. Matsuo, K. Kindo, and H. Tanaka, Magnetization Process and Collective Excitations in the $S=1/2$ Triangular-Lattice Heisenberg Antiferromagnet $Ba_3CoSb_2O_9$, Phys. Rev. Lett. **110**, 267201 (2013).

[61] A. I. Smirnov, H. Yashiro, S. Kimura, M. Hagiwara, Y. Narumi, K. Kindo, A. Kikkawa, K. Katsumata, A. Y. Shapiro, and L. N. Demianets, Triangular lattice antiferromagnet $RbFe(MoO_4)_2$ in high magnetic fields, Phys. Rev. B **75**, 134412 (2007).

[62] J. Hwang, E. S. Choi, F. Ye, C. R. Dela Cruz, Y. Xin, H. D. Zhou, and P. Schlottmann, Successive Magnetic Phase Transitions and Multiferroicity in the Spin-One Triangular-Lattice Antiferromagnet $Ba_3NiNb_2O_9$, Phys. Rev. Lett. **109**, 257205 (2012).

[63] L. Seabra, T. Momoi, P. Sindzingre, and N. Shannon, Phase diagram of the classical Heisenberg antiferromagnet on a triangular lattice in an applied magnetic field, Phys. Rev. B **84**, 214418 (2011).

[64] O. A. Petrenko, G. Balakrishnan, M. R. Lees, D. McK. Paul, and A. Hoser, High-magnetic-field behavior of the triangular-lattice antiferromagnet $CuFeO_2$, Phys. Rev. B **62**, 8983 (2000).

[65] N. Ahmed, A. A. Tsirlin, and R. Nath, Multiple magnetic transitions in the spin-$\frac{1}{2}$ chain antiferromagnet $SrCuTe_2O_6$, Phys. Rev. B **91**, 214413 (2015); Y. C. Arango, E. Vavilova, M. Abdel-Hafiez, O. Janson, A. A. Tsirlin, H. Rosner, S.-L. Drechsler, M. Weil, G. Nénert, R. Klingeler, O. Volkova, A. Vasiliev, V. Kataev, and B. Büchner, Magnetic properties of the low-dimensional spin-$\frac{1}{2}$ magnet α-$Cu_2As_2O_7$, *ibid.* **84**, 134430 (2011).